IJMMM International Journal of Minerals, Metallurgy and Materials 矿物冶金与材料学报（英文版）

Fe-based amorphous coating prepared using high-velocity oxygen fuel and its corrosion behavior in static lead–bismuth eutectic alloy

Xiangyang Peng, Yuhai Tang, Xiangbin Ding, Zhichao Lu, Shuo Hou, Jianming Zhou, Shuyin Han, Zhaoping Lü, Guangyao Lu, and Yuan Wu

Cite this article as:
Xiangyang Peng, Yuhai Tang, Xiangbin Ding, Zhichao Lu, Shuo Hou, Jianming Zhou, Shuyin Han, Zhaoping Lü, Guangyao Lu, and Yuan Wu, Fe-based amorphous coating prepared using high-velocity oxygen fuel and its corrosion behavior in static lead–bismuth eutectic alloy, *Int. J. Miner. Metall. Mater.*, 29(2022), No. 11, pp. 2032-2040. https://doi.org/10.1007/s12613-022-2420-9

Articles you may be interested in

Kuzhipadath Jithesh and Moganraj Arivarasu, Comparative studies on the hot corrosion behavior of air plasma spray and high velocity oxygen fuel coated Co-based L605 superalloys in a gas turbine environment, *Int. J. Miner. Metall. Mater.*, 27(2020), No. 5, pp. 649-659. https://doi.org/10.1007/s12613-019-1943-1

F. Ghadami, A. Sabour Rouh Aghdam, and S. Ghadami, Characterization of MCrAlY/nano-Al_2O_3 nanocomposite powder produced by high-energy mechanical milling as feedstock for high-velocity oxygen fuel spraying deposition, *Int. J. Miner. Metall. Mater.*, 28(2021), No. 9, pp. 1534-1543. https://doi.org/10.1007/s12613-020-2113-1

Li Wang, Chao-fang Dong, Cheng Man, Ya-bo Hu, Qiang Yu, and Xiao-gang Li, Effect of microstructure on corrosion behavior of high strength martensite steel—A literature review, *Int. J. Miner. Metall. Mater.*, 28(2021), No. 5, pp. 754-773. https://doi.org/10.1007/s12613-020-2242-6

Gurmail Singh, Niraj Bala, and Vikas Chawla, Microstructural analysis and hot corrosion behavior of HVOF-sprayed Ni–22Cr–10Al–1Y and Ni–22Cr–10Al–1Y–SiC (N) coatings on ASTM-SA213-T22 steel, *Int. J. Miner. Metall. Mater.*, 27(2020), No. 3, pp. 401-416. https://doi.org/10.1007/s12613-019-1946-y

S.M. Muthu, M. Arivarasu, T. Hari Krishna, Supriyo Ganguly, K.V. Phani Prabhakar, and Saurav Mohanty, Improvement in hot corrosion resistance of dissimilar alloy 825 and AISI 321 CO_2-laser weldment by HVOF coating in aggressive salt environment at 900°C, *Int. J. Miner. Metall. Mater.*, 27(2020), No. 11, pp. 1536-1550. https://doi.org/10.1007/s12613-020-2014-3

Pan-jun Wang, Ling-wei Ma, Xue-qun Cheng, and Xiao-gang Li, Influence of grain refinement on the corrosion behavior of metallic materials: A review, *Int. J. Miner. Metall. Mater.*, 28(2021), No. 7, pp. 1112-1126. https://doi.org/10.1007/s12613-021-2308-0

IJMMM WeChat

QQ author group

International Journal of Minerals, Metallurgy and Materials
Volume 29, Number 11, November 2022, Page 2032
https://doi.org/10.1007/s12613-022-2420-9

Fe-based amorphous coating prepared using high-velocity oxygen fuel and its corrosion behavior in static lead–bismuth eutectic alloy

Xiangyang Peng[1),*], *Yuhai Tang*[2),*], *Xiangbin Ding*[1)], *Zhichao Lu*[2)], *Shuo Hou*[1)], *Jianming Zhou*[1)], *Shuyin Han*[2)], *Zhaoping Lü*[2)], *Guangyao Lu*[1),✉], *and Yuan Wu*[2),✉]

1) Equipment Research Center, China Nuclear Power Technology Research Institute Co., Ltd., Shenzhen 518000, China
2) State Key Laboratory for Advanced Metals and Materials, University of Science & Technology Beijing, Beijing 100083, China
(Received: 28 September 2021; revised: 27 December 2021; accepted: 17 January 2022)

Abstract: The $Fe_{49.7}Cr_{18}Mn_{1.9}Mo_{7.4}W_{1.6}B_{15.2}C_{3.8}Si_2$ amorphous coating was deposited on T91 steel substrate by using the high-velocity oxygen fuel (HVOF) spray technique to enhance the corrosion resistance of T91 stainless steel in liquid lead–bismuth eutectic (LBE). The corrosion behavior of the T91 steel and coating exposed to oxygen-saturated LBE at 400°C for 500 h was investigated. Results showed that the T91 substrate was severely corroded and covered by a homogeneously distributed dual-layer oxide on the interface contacted to LBE, consisting of an outer magnetite layer and an inner Fe–Cr spinel layer. Meanwhile, the amorphous coating with a high glass transition temperature (T_g = 550°C) and crystallization temperature (T_x = 600°C) exhibited dramatically enhanced thermal stability and corrosion resistance. No visible LBE penetration was observed, although small amounts of Fe_3O_4, Cr_2O_3, and PbO were found on the coating surface. In addition, the amorphicity and interface bonding of the coating layer remained unchanged after the LBE corrosion. The Fe-based amorphous coating can act as a stable barrier layer in liquid LBE and have great application potential for long-term service in LBE-cooled fast reactors.

Keywords: Fe-based amorphous coating; high-velocity oxygen fuel; corrosion behavior; lead–bismuth eutectic

1. Introduction

Lead–bismuth eutectic (LBE) is a promising candidate material for core coolants in accelerator-driven sub-critical systems because of its excellent thermal-physical properties and high neutron economy [1]. However, the application of LBE is limited by its compatibility with structural materials, especially at high temperatures [2–4]. During operation, structural materials suffer severe oxidation corrosion or elemental dissolution [5]. As a result, the surface morphology, microstructure, and structure of the materials are vulnerable to being changed, which consequently deteriorates the mechanical properties of structural materials and eventually causes material failure under working conditions [6–16].

Several approaches have been proposed to form protective coatings on the surface of structural materials, such as T91 and 316L steels, to alleviate LBE corrosion. A typical method is to form protective nitride and carbide films on the steel surface by adding alloying elements, such as Zr or Ti, into the LBE liquids to form insoluble films of ZrN, TiN, or TiC and then enhance protection to a certain degree [17–20]. Another means is to control the dissolved oxygen content in LBE to obtain stable oxide layers on the surface of structural materials [21–24]. Although some favorable results have been achieved by using the above methods, protective films are difficult to control because they are affected by many factors, such as flow velocity, temperature, and oxygen concentration. Therefore, other effective protection methods that can directly modify the surface of structural materials are urgently required.

Preparation of protective coatings on the surface of structural materials is an effective measure to alleviate LBE corrosion. Several coating materials, including refractory metal coatings (Mo, Nb, and W) [25], alloy coatings (FeCrAl, FeAlTi, and FeAl) [26–28], ceramic coatings (TiN, CrN, Al_2O_3, SiC, and Ti_3SiC_2) [19,25,29], and composite coatings (SiC/SiC and sol–gel composites) [30–31], have already been developed. Although these coatings exhibit good corrosion resistance, issues such as the easily formed grain defects promote the permeation of LBE along the grain boundary, causing material failure during long-term experiments. The complex preparation process also increases the cost of practical applications. Therefore, it remains challenging to develop coating materials that can endure aggressive corrosion and possess the potential for industrial applications in advanced nuclear reactors.

Amorphous alloys have a long-range disordered atomic packing structure and contain no crystalline defects, such as

*These authors contributed equally to this work.
✉ Corresponding authors: Guangyao Lu E-mail: Luguangyao@cgnpc.com.cn; Yuan Wu E-mail: wuyuan@ustb.edu.cn

grain boundaries, which are prone to corrosion as in crystalline materials. Therefore, they have a unique combination of favorable properties, such as high hardness, excellent wear, and good corrosion resistance [32]. In specific, Fe-based amorphous coatings (Fe-AC) are extremely practical candidates of surface protective barriers in LBE owing to their high crystallization temperature, predominant corrosion resistance, and relatively low fabrication cost [33–35]. Among various fabrication techniques, HVOF (high-velocity oxygen fuel) is an economical and frequently used approach to develop surface coatings because of its high cooling rate (10^7–10^{10} K·s^{-1}) and favorable properties, such as low porosity, high hardness, lower oxide content, and high adhesion strength [36–39]. However, the corrosion behavior of Fe-AC in LBE liquids remains unclear.

In this study, the $Fe_{49.7}Cr_{18}Mn_{1.9}Mo_{7.4}W_{1.6}B_{15.2}C_{3.8}Si_2$ amorphous coating was deposited on T91 steel substrate through HVOF, and the microstructure, glass-forming ability, and thermal stability of the coating were investigated. The corrosion behavior of the T91 substrate and Fe-AC in static oxygen-saturated LBE at 400°C was observed, which suggests that the current Fe-based amorphous coating exhibits excellent corrosion resistance in liquid LBE and has great potential to be utilized as a corrosion-resistant coating in accelerator-driven systems and advanced nuclear reactors.

2. Experimental

2.1. Preparation of alloy powder and amorphous coating

The $Fe_{49.7}Cr_{18}Mn_{1.9}Mo_{7.4}W_{1.6}B_{15.2}C_{3.8}Si_{2.4}$ (at%) alloy ingot was prepared by the induction melting of Fe (99.9wt%), Cr (99.5wt%), Mn (99.9wt%), Mo (99.9wt%), W (99.9wt%), C (99.9wt%), and Fe–B (B 23wt%, Fe 74wt%, Si 2wt%) in an argon atmosphere. From the master alloy, ribbon samples were produced by a single-roller melt-spinning technique for calculating the amorphous content of the coatings. Amorphous powders with the same composition were prepared by high-pressure Ar gas atomization, and then as-atomized powders with sizes in the range of 30–50 μm were sieved following conventional sieve analysis. The T91 substrates were degreased by acetone, dried in air, grit-blasted with a mean surface roughness (R_a) of approximately 4 μm, and then preheated at 120°C before spraying. For the HVOF process, the ZB-2000 HVOF spraying system (Beijing Zhen Bang Aerospace Precision Machinery Co., Ltd., China) was adopted with the following parameters: kerosene flow of 30–32 L/min, oxygen flow of 52 L/min, powder-feed rate of 75 g/min, and barrel length of 380 mm.

2.2. Microstructure characterization

The microstructure of the powders and coatings was characterized using scanning electron microscopy (SEM; SUPRA55, Carl Zeiss Jena, Germany) equipped with energy dispersive spectroscopy (EDS). X-ray diffraction (XRD; X' pert APD, Philips, Holland) and transmission electron microscopy (TEM; JEM-2100, JEOL, Japan) were performed to analyze the structure of the substrate and the coating. Glass transition temperatures and crystallization enthalpy of the powder, coating, and ribbon were characterized using differential scanning calorimetry (DSC; STA499-C, NETZSCH Co., Germany) at a heating rate of 20°C/min under Ar atmosphere. The crystallized volume fraction of the as-atomized powders and Fe-AC was estimated by normalizing them with the crystallization enthalpy of the ribbons. In addition, the porosity of Fe-AC was calculated using Image-Pro in accordance with ASTM E2109–01, and ten images were selected to obtain accurate results. The bond strength between the coating and the substrate was measured using a universal testing machine (WDW-100E, Panasonic, Japan) with a tensile speed of 1 mm/min in accordance with GB/T 8642–2002. The final value was obtained after averaging at least two measurements.

2.3. Vickers hardness test

Vickers hardness (HV) of the substrate and amorphous coating before and after corrosion was measured at a load of 200 g and a loading time of 15 s by using a Vickers hardness testing system (Hmicro-Vickers indenter, Wolpert-401MVD, Buehler Ltd., American).

2.4. LBE corrosion test

In this study, static LBE corrosion tests were carried out in a tubular furnace under an oxygen-saturated atmosphere, which could simulate the serving environment in the nuclear industry. The temperature of the LBE liquid was set at 400°C, and the immersion period for the specimens (the coated T91 and the bare T91 for reference) was set for 500 h. After the LBE corrosion testing, the samples were rinsed in a solution containing hydrogen peroxide, acetic acid, and ethyl alcohol with a volume ratio of 1:1:1 to remove LBE stuck from the sample surface. Inevitably, adherent LBE liquid was left on a few parts of the sample surface. The cross-section and the surface of the coated T91 substrate were observed using SEM with EDS. The surface valence state of Fe-AC after LBE corrosion was characterized using X-ray photoelectron spectroscopy (XPS, AXIS-ULTRA-DLD, Kratos).

3. Results and discussion

3.1. Microstructure characterization

The microstructure of the as-atomized powders is shown in Fig. 1(a). Most of the particles are spherical or near-spherical in shape despite some satellite-shaped powders. The majority of the powders exhibit smooth surfaces, indicating good fluidity during the spraying process. The particle size distribution of the atomized powders shown in Fig. 1(b) follows a typical Gaussian distribution, and the size of most particles is between 30 and 50 μm. XRD patterns of the atomized powders and Fe-AC are shown in Fig. 1(c). The single broad halo imposed with several small crystalline peaks hump reveals that the as-atomized powders have an amorphous structure with the co-existence of a few $Fe_{23}(C,B)_6$ particles. The crystallization peaks are pro-

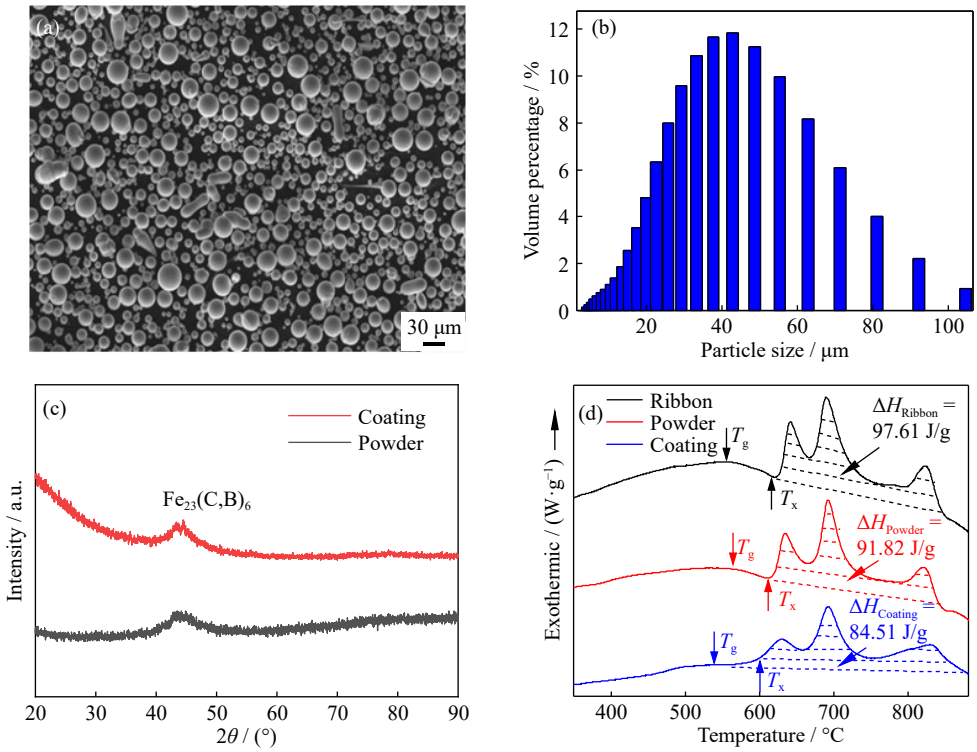

Fig. 1. Powder morphology (a) and particle size distribution (b) of the as-atomized Fe-AC powders. (c) XRD patterns of the atomized powders and the as-sprayed coating. (d) DSC curves of the power, melt-spun ribbon, and as-sprayed coating.

nounced in the as-sprayed coatings, which can be attributed to the crystallization during the HVOF process. The DSC traces of the amorphous powder, ribbon, and the as-spayed coating are shown in Fig.1(d). All the specimens show a similar crystallization process with three exothermic peaks. The glass transition temperature (T_g) and the onset crystallization temperature (T_x) of the coating are approximately 550 and 600°C, respectively, which are higher than the serving environment in the nuclear industry. The volume fraction (vol%) of the amorphous phase in the powders and coatings was estimated by comparing their heat of crystallization (ΔH) value with that of the ribbon reference sample. The amorphous contents of the powder and the coating are approximately 94% and 87%, respectively, which are consistent with the XRD results.

$$\text{Volume fraction} = \frac{\Delta H_{\text{Powder/coating}}}{\Delta H_{\text{Ribbon}}} \quad (1)$$

A cross-sectional examination of the coating was carried out using SEM (Fig. 2(a)). The amorphous coating formed a good bonding with the T91 steel substrate, and the coating itself showed a dense and uniform structure with a mean thickness of 340 μm and a porosity of 0.984%, as observed in Fig. 2(b). The average tensile bond strength between the Fe-AC powders and T91 substrate was measured to be 53 MPa. EDS line scanning diagram (Fig. 2(c)) and EDS maps (Fig. 2(d)) show that the elements in the coating are distributed uniformly, except for slight fluctuations in Fe and O, which may be caused by crystallization and oxidation during coating preparation. The coating surface is unevenly concave with a large number of particles staggered and stacked together (Fig. 3(a)), and some pores and micro-cracks still exist after polishing (Fig. 3(b)), which are typical for an HVOF-sprayed coating.

TEM characterization was applied to acquire detailed structural information of the specimens. Good metallurgical bonding between the coating and the T91 substrate can be observed in Fig. 4. The inset diffused halo ring of the selected area diffraction (SAED) pattern (position #I) in the upper right corner shows that the matrix still retains its crystal structure, whereas the SAED pattern (position #II) on the left bottom verifies that the coating is mainly composed of the amorphous phase. Regarding the left side of position II, it is also the as-prepared coating, which is far from the substrate and the interface. As shown in the TEM image, the atoms in the left region pack in a disordered manner, indicating that the coating has a good amorphous structure.

3.2. Corrosion behavior in the static LBE liquid

The bare T91 steel substrate was also immersed in the same LBE corrosion conditions for comparison to elucidate the LBE corrosion resistance of the amorphous coating. As shown in Figs. 5 and 6, the surface of the T91 specimen after the experiment is covered by a homogeneously distributed oxide layer with a thickness ranging from 6 to 10 μm, indicating that severe oxidation corrosion occurred within the uncoated steel. The elemental distributions in the oxide films in Fig. 6(b) reveal that the Cr content in the inner oxide film is higher than that in the outer one, while the Fe element has an opposite trend. Therefore, the oxide layer consists of two zones with different Cr contents. Previous studies [4,40] showed that the inner oxide film with a compact structure is mainly composed of $(Fe,Cr)_3O_4$, whereas the porous outer

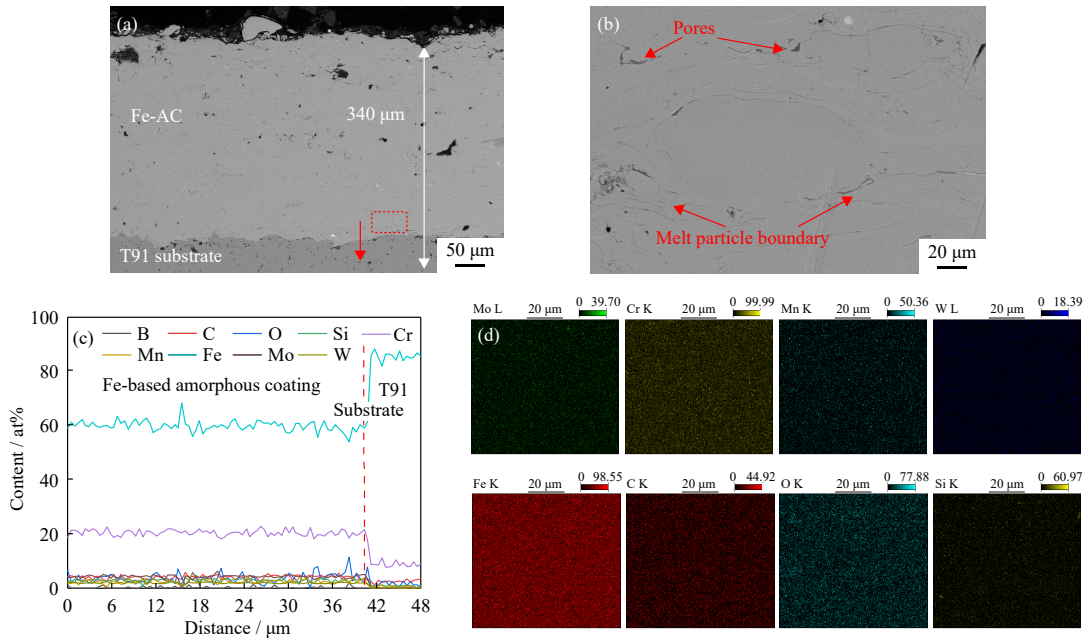

Fig. 2. (a) Cross-sectional SEM images of the amorphous coating prepared by HVOF, (b) a close-up in the rectangular region in (a), (c) EDS line scan along the red line in (a), and (d) EDS mapping of the coating corresponding to (b).

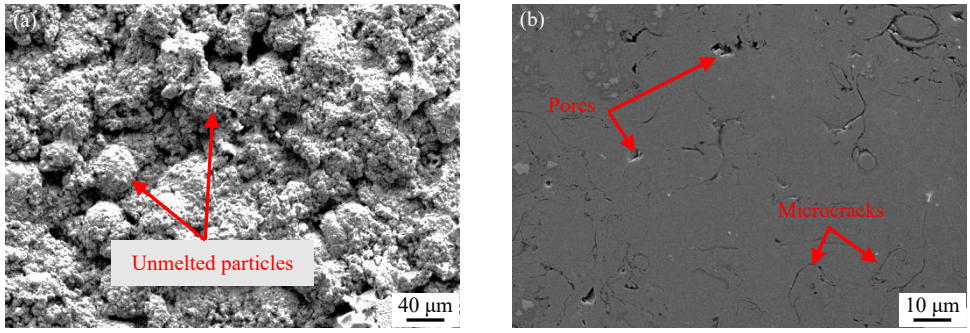

Fig. 3. Surface morphology of Fe-AC: (a) as-sprayed and (b) after polishing.

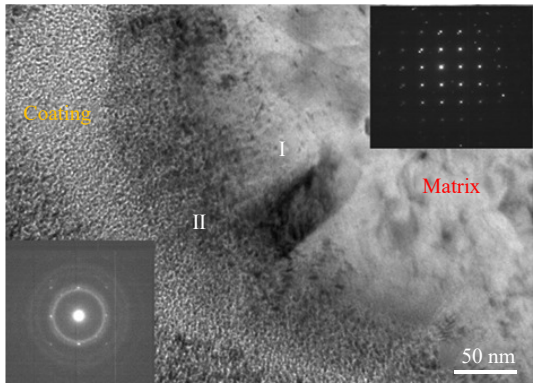

Fig. 4. Bright-field TEM image of the coated T91; SAED patterns of the T91 substrate (position #I) and the interface between the coating and substrate (position #II).

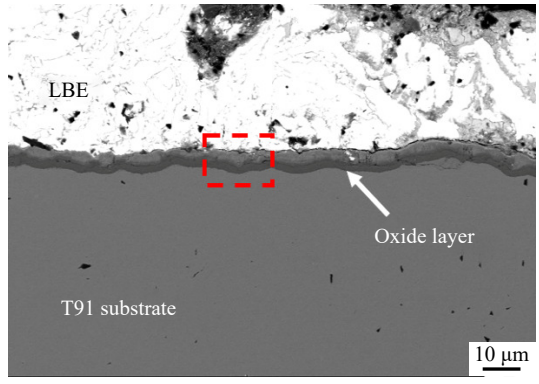

Fig. 5. SEM cross-sectional image of T91 after exposure in static LBE at 400℃ for 500 h.

oxide film is mainly composed of Fe_3O_4. The formation mechanism of the duplex oxide layer is not fully elucidated at present, and the diffusion coefficient difference in the alloy may contribute to the occurrence of this phenomenon. Experimental results [41] demonstrated that the diffusion coefficient of Fe is much higher than that of Cr in the Fe–Cr spinel oxide layer. The amount of Cr diffused to the steel surface is insufficient to form more spinel, and Fe_3O_4 emerges because of the high oxygen concentration within the LBE medium. The growth of the outer Fe_3O_4 is associated with the transfer of the Fe element outward, whereas the inner Fe–Cr spinel film develops with the movement of oxide through the oxide film [42]. The oxidation process is controlled by the outer layer growth, and the inner spinel film occupies the space caused by consuming the original steel constituents.

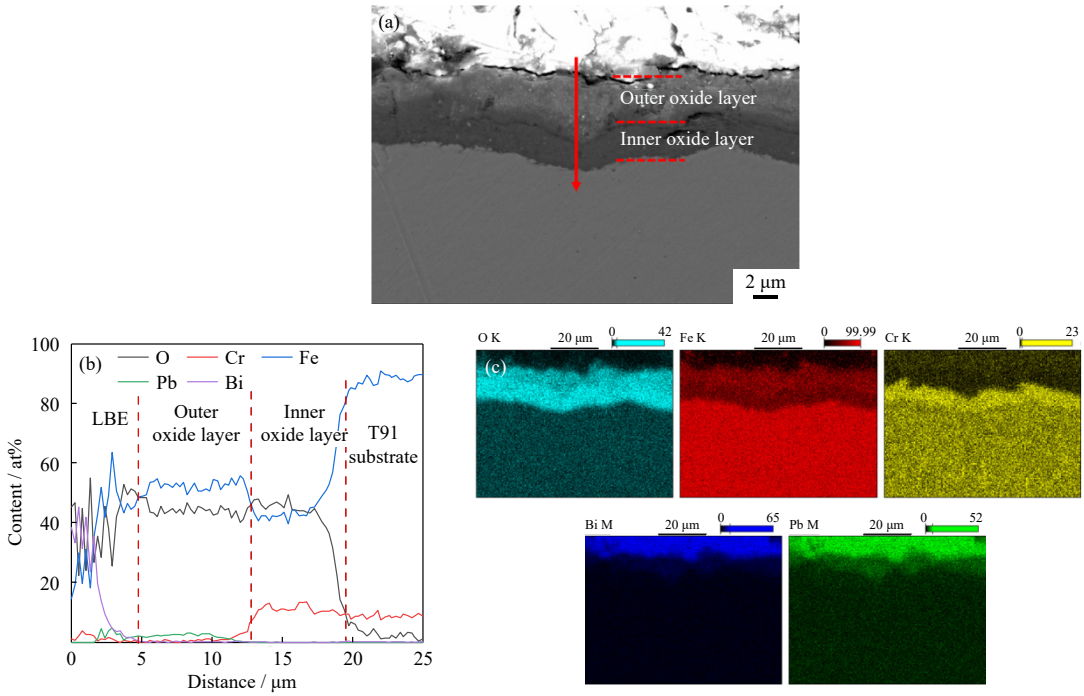

Fig. 6. (a) Cross-sectional SEM image of bare T91 after exposure to the LBE liquid at 400℃ for 500 h. (b) EDS line scan and (c) EDS mapping of oxide layer along the red line in (a).

Fig. 7(a) displays the cross-sectional image of the coated T91 after LBE corrosion. Clearly, the coating layer remained continuous and uniform, and neither obvious morphological changes nor thickness changes occurred. As shown in Fig. 7(b), the number of unmelted particles reduced, as compared with Fig. 3(a). The chemical composition of the protective layer after the corrosion tests was determined through EDS, as shown in Fig. 7(c). All elements were homogeneously distributed in the amorphous coating, and no significant chemical change was observed on the as-sprayed samples after corrosion. In addition, the oxide layer did not form on the surface appreciably, and no penetration of LBE liquid into the coating was detected. In Fig. 7(d), XRD spectra of the coating still shows a typical diffuse hump indicative of an amorphous structure. The low content of the crystalline phase remained low, and no precipitation of any other new crystalline phases was found inside the coating.

XPS tests were carried out on the surface of the samples after cleaning the residual LBE to determine the surface composition of the amorphous coating after static corrosion. In

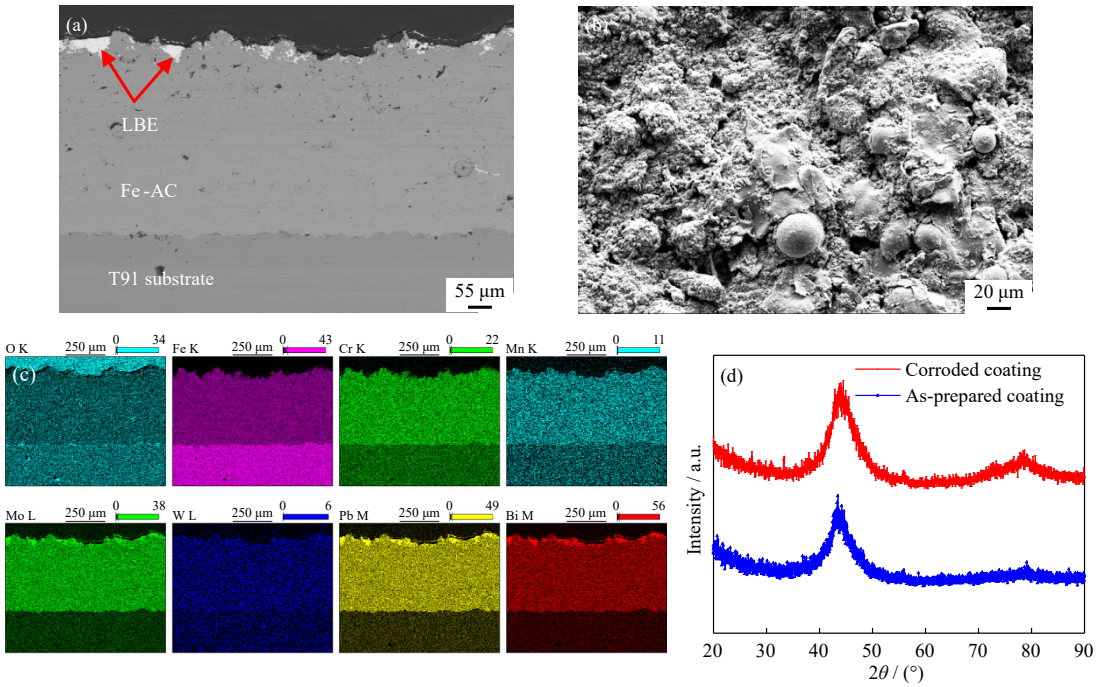

Fig. 7. Cross-sectional SEM image of the as-prepared coating after exposure to the LBE liquid at 400℃ for 500 h (a), surface morphology (b) and EDS mapping results (c) of the coating, and XRD patterns before and after corrosion (d).

our test, the peak of C 1s from the experimental data was 284.7 eV. The high-resolution XPS spectra of the Fe-AC samples (Fe 2p, Cr 2p, Pb 4f, and O 1s) after corrosion are shown in Fig. 8. The XPS spectra of Fe 2p in Fig. 8(a) show that the Fe $2p_{3/2}$ spectrum could be fitted with two peaks, one at 710.7 eV corresponding to Fe^{2+} and another at 712.7 eV corresponding to Fe^{3+} [43]. The Cr 2p XPS spectrum in Fig. 8(b) displays double peaks at 576.9 and 586.8 eV, which are recognized as the peaks of Cr^{3+}, indicating the formation of Cr_2O_3 [44]. The spectrum of Pb 4f proves the existence of the oxidation state of Pb, which has two peaks fitted at 138.0 and 142.9 eV, belonging to PbO [45]. In addition, analysis of the O 1s spectrum displayed two peaks situated at 530.3 and 531.6 eV, which correspond to Fe_3O_4 and PbO [45–46]. The XPS analysis suggests that the oxide layer consisting of Fe_3O_4, Cr_2O_3, and PbO may form on the coating surface. The microscale oxide layer can improve the corrosion resistance of Fe-based amorphous coating [47–48]. Therefore, no obvious LBE permeation and elemental dissolution were observed on the Fe-AC surface in Fig. 7(a).

Structural characterization of the amorphous coating and the interface between the coating and the substrate after the static LBE corrosion test was investigated by TEM (Fig. 9). Excellent metallurgical bonding still existed (position #III) between the T91 steel substrate and the amorphous coating after the LBE corrosion, and the coating still maintained a good amorphous structure, as indicated by the diffraction ring in Fig. 9(b). The SAED pattern (Fig. 9(c)) of the T91 matrix (position #II) still retained the crystal structure, although a small amount of amorphous structure appeared. This result can be ascribed to the selected area being close to the coating (not fully peeled off from the substrate). The results above prove that the amorphous coating can protect the matrix material for a long time in the LBE medium.

The observed beneficial effects can be attributed to the specific composition and unique atomic structure of the amorphous coating. From the standpoint of structure, Fe-AC was prepared through the rapidly cooling method so that no grain boundaries, dislocations, or other physical imperfections existed in the amorphous phase, reducing the probabil-

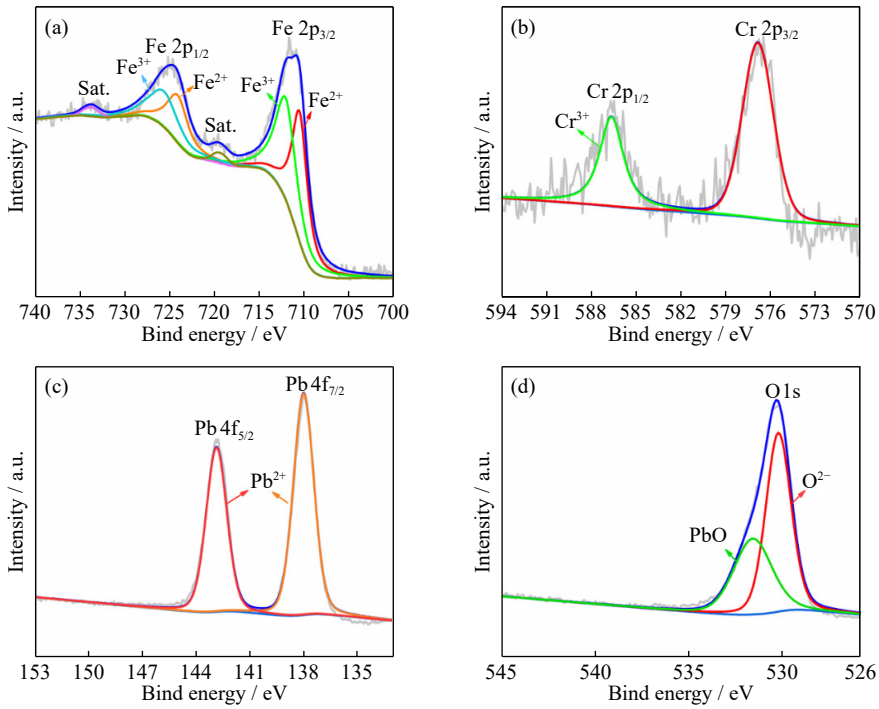

Fig. 8. XPS results about the surface of Fe-AC after exposure in static LBE: (a) Fe 2p analysis, (b) Cr 2p analysis, (c) Pb 4f analysis, and (d) O 1s analysis.

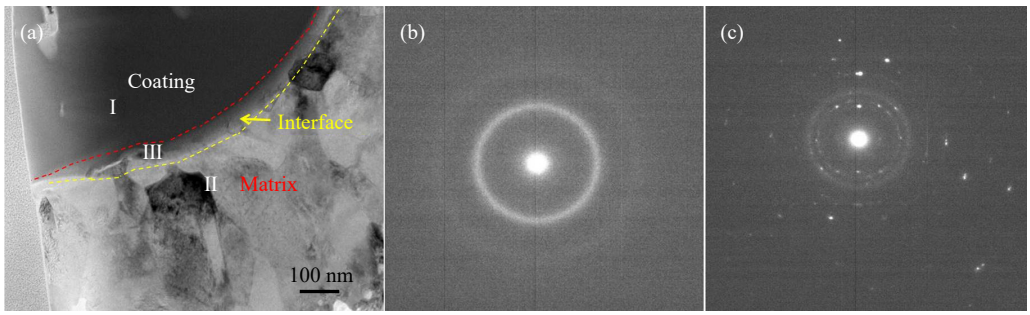

Fig. 9. (a) Cross-sectional TEM images of the amorphous coating corroded at 400℃ for 500 h, (b) diffraction pattern of coating (position #I), and (c) diffraction pattern of the T91 (position #II).

ity of alloy elements being dissolved or replaced at these crystalline defects and the chance of intergranular corrosion. Grain boundaries are a fast channel of oxidation corrosion. The long-range disordering structure of the amorphous coating can alleviate or even avoid oxidation corrosion, which contributes to the fact that no oxide layer formed appreciably on the coating surface. As mentioned earlier, slight corrosion occurred in the amorphous coating, which was mainly due to the damage in the continuity of the microstructure resulting from the existence of the crystalline phases. Therefore, enhancing the glass formation ability and surface quality of the amorphous coating may further improve the protection capability of the amorphous coating.

The possible corrosion mechanism of Fe-AC in LBE at 400°C for 500 h is shown in Fig. 10. A very thin corrosion layer emerged because of the low diffusion rate of the elements in the coating (caused by the long-range disordering structure) and the short corrosion time. When Fe-AC was immersed in high-temperature LBE, O atoms in LBE diffused rapidly into the coating surface, and the Fe and Cr atoms in Fe-AC diffused outward. First, the O atoms reacted with Fe to generate an outer Fe_3O_4 because of the high diffusion rate of Fe atoms. As the oxygen atoms continued to diffuse, Cr_2O_3 nodules formed underneath the Fe_3O_4 oxide layer. Then, the Cr-rich nodules grew inward and gradually connected to generate a continuous Cr-rich layer, which restrained the diffusion of oxygen and metal elements.

3.3. Vickers hardness

The hardness of the substrate and the coating was measured to investigate the evolution of mechanical behavior of Fe-AC. Vickers hardness images of the amorphous coating before and after corrosion in static LBE are shown in Fig. 11. The hardness of the amorphous coating ($HV_{0.2}$ 983 on aver-

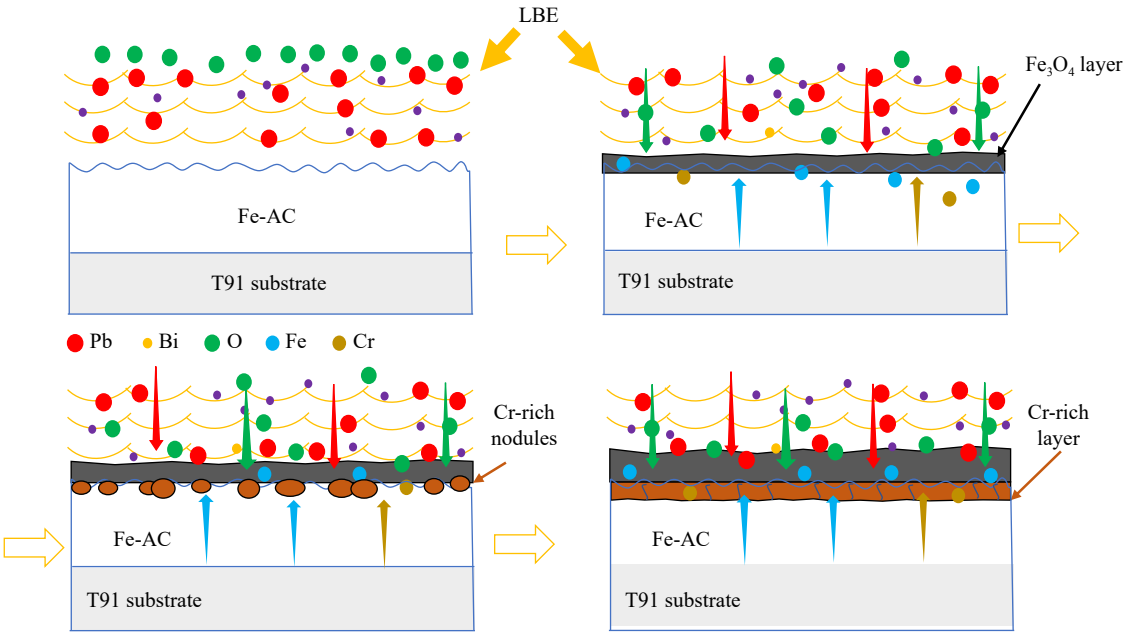

Fig. 10. Corrosion mechanism of Fe-AC in LBE at 400℃ for 500 h.

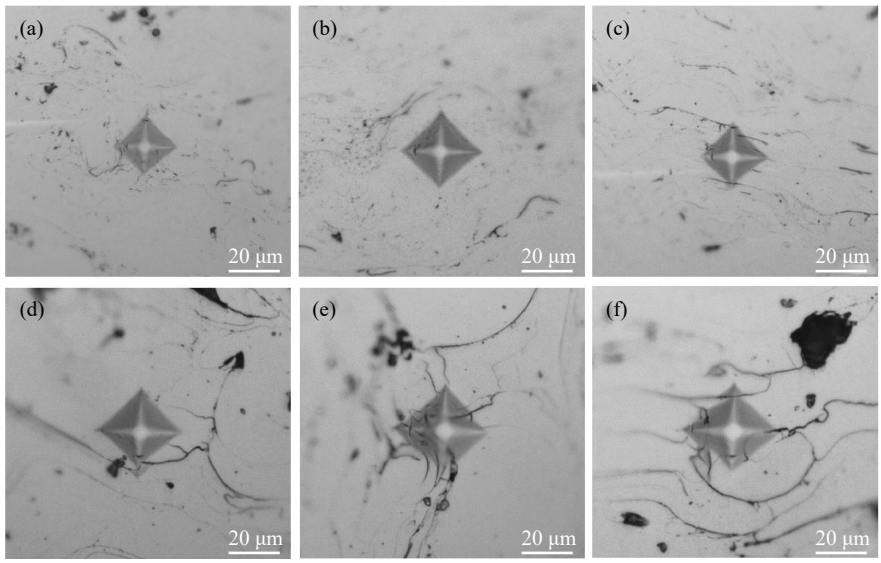

Fig. 11. Vickers hardness images of the amorphous coating: (a–c) as-sprayed and (d–f) after LBE corrosion test.

age) was significantly higher than that of the bare T91 ($HV_{0.2}$ 170). This result can be ascribed to the effect of melted particles carried by argon on the T91 substrate with extremely high kinetic energy and heat, resulting in severe shape deformation of powder particles and the interface between the coating and the substrate, thereby increasing the hardness of the coating. After the LBE corrosion testing, the hardness of the coating ($HV_{0.2}$ 773 on average) decreased slightly, but it was still much higher than the hardness of the substrate, which also proved that no visible corrosion product was generated on the surface and further verified the good corrosion resistance of Fe-AC in the LBE medium.

4. Conclusion

In this work, the $Fe_{49.7}Cr_{18}Mn_{1.9}Mo_{7.4}W_{1.6}B_{15.2}C_{3.8}Si_{2.4}$ amorphous coating as a barrier against LBE corrosion was successfully prepared using the HVOF method. The as-sprayed amorphous coating presents a dense and homogeneous structure with high hardness and good interface adhesion. Fe-AC exhibits good anti-LBE corrosion resistance with much lower consumption of the coating as compared with the bare T91 steel under the same corrosive conditions. The long-range disordered structure in Fe-AC may contribute to the high LBE corrosion resistance. The amorphicity and interface bonding remain unchanged after the static LBE corrosion, indicating that the amorphous coating has great potential for long-term service in LBE-cooled fast reactors.

Acknowledgements

The work was financially supported by the National Natural Science Foundation of China (Nos. 52061135207, 51871016, 51921001, 5197011039, 5197011018, and U20b200318) and the China Nuclear Power Technology Research Institute Co., Ltd.

Conflict of interest

The authors declare that they have no conflicts of interest in this work.

References

[1] K.L. Murty and I. Charit, Structural materials for Gen-IV nuclear reactors: Challenges and opportunities, *J. Nucl. Mater.*, 383(2008), No. 1-2, p. 189.

[2] H. Wang, J. Xiao, H. Wang, *et al*., Corrosion behavior and surface treatment of cladding materials used in high-temperature lead–bismuth eutectic alloy: A review, *Coatings*, 11(2021), No. 3, p. 364.

[3] J.S. Zhang and N. Li, Review of the studies on fundamental issues in LBE corrosion, *J. Nucl. Mater.*, 373(2008), No. 1-3, p. 351.

[4] J.S. Zhang, A review of steel corrosion by liquid lead and lead-bismuth, *Corros. Sci.*, 51(2009), No. 6, p. 1207.

[5] J.S. Zhang and N. Li, Analysis on liquid metal corrosion–oxidation interactions, *Corros. Sci.*, 49(2007), No. 11, p. 4154.

[6] V. Tsisar, S. Gavrilov, C. Schroer, and E. Stergar, Long-term corrosion performance of T91 ferritic/martensitic steel at 400°C in flowing Pb–Bi eutectic with 2×10^{-7} mass% dissolved oxygen, *Corros. Sci.*, 174(2020), p. 108852.

[7] I. Proriol Serre, I. Diop, N. David, M. Vilasi, and J.B. Vogt, Mechanical behavior of coated T91 steel in contact with lead-bismuth liquid alloy at 300°C, *Surf. Coat. Technol.*, 205(2011), No. 19, p. 4521.

[8] G. Müller, A. Heinzel, J. Konys, *et al*., Results of steel corrosion tests in flowing liquid Pb/Bi at 420–600°C after 2000 h, *J. Nucl. Mater.*, 301(2002), No. 1, p. 40.

[9] A. Weisenburger, C. Schroer, A. Jianu, *et al*., Long term corrosion on T91 and AISI1 316L steel in flowing lead alloy and corrosion protection barrier development: Experiments and models, *J. Nucl. Mater.*, 415(2011), No. 3, p. 260.

[10] G. Benamati, A. Gessi, and P.Z. Zhang, Corrosion experiments in flowing LBE at 450°C, *J. Nucl. Mater.*, 356(2006), No. 1-3, p. 198.

[11] F. Gnecco, E. Ricci, C. Bottino, and A. Passerone, Corrosion behaviour of steels in lead–bismuth at 823 K, *J. Nucl. Mater.*, 335(2004), No. 2, p. 185.

[12] A. Aiello, M. Azzati, G. Benamati, A. Gessi, B. Long, and G. Scaddozzo, Corrosion behaviour of stainless steels in flowing LBE at low and high oxygen concentration, *J. Nucl. Mater.*, 335(2004), No. 2, p. 169.

[13] J.S. Zhang, N. Li, Y. Chen, and A.E. Rusanov, Corrosion behaviors of US steels in flowing lead–bismuth eutectic (LBE), *J. Nucl. Mater.*, 336(2005), No. 1, p. 1.

[14] Y. Kurata, M. Futakawa, and S. Saito, Corrosion behavior of steels in liquid lead–bismuth with low oxygen concentrations, *J. Nucl. Mater.*, 373(2008), No. 1-3, p. 164.

[15] A. Doubková, F. di Gabriele, P. Brabec, and E. Keilová, Corrosion behavior of steels in flowing lead–bismuth under abnormal conditions, *J. Nucl. Mater.*, 376(2008), No. 3, p. 260.

[16] C. Fazio, G. Benamati, C. Martini, and G. Palombarini, Compatibility tests on steels in molten lead and lead–bismuth, *J. Nucl. Mater.*, 296(2001), No. 1-3, p. 243.

[17] E.P. Loewen, H.J. Yount, K. Volk, and A. Kumar, Layer formation on metal surfaces in lead–bismuth at high temperatures in presence of zirconium, *J. Nucl. Mater.*, 321(2003), No. 2-3, p. 269.

[18] O.F. Kammerer, J.R. Weeks, J. Sadofsky, W.E. Miller, and D.H. Gurinsky, Zirconium and titanium inhibit corrosion and mass transfer of steels by liquid heavy metals, *Trans. Met. Soc. AIME*, 212(1958), No. 1, art. No. 4306436.

[19] H. Glasbrenner and F. Gröschel, Exposure of pre-stressed T91 coated with TiN, CrN and DLC to Pb-55.5Bi, *J. Nucl. Mater.*, 356(2006), No. 1-3, p. 213.

[20] J.R. Weeks and C.J. Klamut, Reactions between steel surfaces and zirconium in liquid bismuth, *Nucl. Sci. Eng.*, 8(1960), No. 2, p. 133.

[21] N. Li, Active control of oxygen in molten lead–bismuth eutectic systems to prevent steel corrosion and coolant contamination, *J. Nucl. Mater.*, 300(2002), No. 1, p. 73.

[22] L. Martinelli, C. Jean-Louis, and B.C. Fanny, Oxidation of steels in liquid lead bismuth: Oxygen control to achieve efficient corrosion protection, *Nucl. Eng. Des.*, 241(2011), No. 5, p. 1288.

[23] G. Müller, A. Heinzel, G. Schumacher, and A. Weisenburger, Control of oxygen concentration in liquid lead and lead–bismuth, *J. Nucl. Mater.*, 321(2003), No. 2-3, p. 256.

[24] J. Lim, G. Manfredi, S. Gavrilov, K. Rosseel, A. Aerts, and J. Van den Bosch, Control of dissolved oxygen in liquid LBE by electrochemical oxygen pumping, *Sens. Actuators B*, 204(2014), p. 388.

[25] A.K. Rivai and M. Takahashi, Compatibility of surface-coated steels, refractory metals and ceramics to high temperature lead–bismuth eutectic, *Prog. Nucl. Energy*, 50(2008), No. 2-6,

p. 560.
[26] E. Yamaki-Irisawa, S. Numata, and M. Takahashi, Corrosion behavior of heat-treated Fe–Al coated steel in lead–bismuth eutectic under loading, *Prog. Nucl. Energy*, 53(2011), No. 7, p. 1066.
[27] Y. Kurata, H. Yokota, and T. Suzuki, Development of aluminum-alloy coating on type 316SS for nuclear systems using liquid lead–bismuth, *J. Nucl. Mater.*, 424(2012), No. 1-3, p. 237.
[28] R. Fetzer, A. Weisenburger, A. Jianu, and G. Müller, Oxide scale formation of modified FeCrAl coatings exposed to liquid lead, *Corros. Sci.*, 55(2012), p. 213.
[29] F. García Ferré, M. Ormellese, F. Di Fonzo, and M.G. Beghi, Advanced Al_2O_3 coatings for high temperature operation of steels in heavy liquid metals: A preliminary study, *Corros. Sci.*, 77(2013), p. 375.
[30] R. Kasada and P. Dou, Sol–gel composite coatings as anti-corrosion barrier for structural materials of lead–bismuth eutectic cooled fast reactor, *J. Nucl. Mater.*, 440(2013), No. 1-3, p. 647.
[31] X.Z. Fan, W.Z. Huang, H.T. Liu, and H.F. Cheng, Bond stability and oxidation resistance of BSAS-based coating on C/SiC composites, *Surf. Coat. Technol.*, 309(2017), p. 35.
[32] H.X. Li, Z.C. Lu, S.L. Wang, Y. Wu, and Z.P. Lu, Fe-based bulk metallic glasses: Glass formation, fabrication, properties and applications, *Prog. Mater. Sci.*, 103(2019), p. 235.
[33] H.Y. Yuan, H.M. Zhai, W.S. Li, *et al*., Study of dry sliding wear behavior of a Fe-based amorphous coating synthesized by detonation spraying on an AZ31B magnesium alloy, *J. Mater. Eng. Perform.*, 30(2021), No. 2, p. 905.
[34] Z. Lu, X. Chen, X. Liu, *et al*., Interpretable machine-learning strategy for soft-magnetic property and thermal stability in Fe-based metallic glasses, *npj Comput. Mater.*, 6(2020), No. 1, p. 1.
[35] Z.C. Lu, X.Y. Peng, Y.H. Tang, *et al*., Corrosion and irradiation behavior of Fe-based amorphous coating in lead–bismuth eutectic liquids, *Sci. China: Technol. Sci.*, 65(2022), No. 2, p. 440.
[36] J.F. Zhang, M. Liu, J.B. Song, C.M. Deng, and C.G. Deng, Microstructure and corrosion behavior of Fe-based amorphous coating prepared by HVOF, *J. Alloys Compd.*, 721(2017), p. 506.
[37] S.M. Muthu, M. Arivarasu, T.H. Krishna, *et al*., Improvement in hot corrosion resistance of dissimilar alloy 825 and AISI 321 CO_2-laser weldment by HVOF coating in aggressive salt environment at 900°C, *Int. J. Miner. Metall. Mater.*, 27(2020), No. 11, p. 1536.
[38] C. Zhang, L. Liu, K.C. Chan, Q. Chen, and C.Y. Tang, Wear behavior of HVOF-sprayed Fe-based amorphous coatings, *Intermetallics*, 29(2012), p. 80.
[39] G. Singh, N. Bala, and V. Chawla, Microstructural analysis and hot corrosion behavior of HVOF-sprayed Ni–22Cr–10Al–1Y and Ni–22Cr–10Al–1Y–SiC(N) coatings on ASTM-SA213-T22 steel, *Int. J. Miner. Metall. Mater.*, 27(2020), No. 3, p. 401.
[40] C.F. Yao, H.P. Zhang, H.L. Chang, *et al*., Structure of surface oxides on martensitic steel under simultaneous ion irradiation and molten LBE corrosion, *Corros. Sci.*, 195(2022), art. No. 109953.
[41] J.D. Hodge, Diffusion of chromium in magnetite as a function of oxygen partial pressure, *J. Electrochem. Soc.*, 125(1978), No. 2, p. 55C.
[42] M.G.C. Cox, B. McEnaney, and V.D. Scott, Phase interactions in the growth of thin oxide films on iron–chromium alloys, *Philos. Mag. A: J. Theor. Exp. Appl. Phys.*, 29(1974), No. 3, p. 585.
[43] V. Maurice, W.P. Yang, and P. Marcus, X-ray photoelectron spectroscopy and scanning tunneling microscopy study of passive films formed on (100) Fe–18Cr–13Ni single-crystal surfaces, *J. Electrochem. Soc.*, 145(1998), No. 3, p. 909.
[44] G.C. Allen, S.J. Harris, J.A. Jutson, and J.M. Dyke, A study of a number of mixed transition metal oxide spinels using X-ray photoelectron spectroscopy, *Appl. Surf. Sci.*, 37(1989), No. 1, p. 111.
[45] S. Rondon and P.M.A. Sherwood, Core level and valence band spectra of PbO_2 by XPS, *Surf. Sci. Spectra*, 5(1998), No. 2, p. 104.
[46] C.D. Wagner, D.A. Zatko, and R.H. Raymond, Use of the oxygen KLL Auger lines in identification of surface chemical states by electron spectroscopy for chemical analysis, *Anal. Chem.*, 52(1980), No. 9, p. 1445.
[47] J.J. Si, X.H. Chen, Y.H. Cai, Y.D. Wu, T. Wang, and X.H. Hui, Corrosion behavior of Cr-based bulk metallic glasses in hydrochloric acid solutions, *Corros. Sci.*, 107(2016), p. 123.
[48] S.J. Pang, T. Zhang, K. Asami, and A. Inoue, Formation of bulk glassy $Fe_{75-x-y}Cr_xMo_yC_{15}B_{10}$ alloys and their corrosion behavior, *J. Mater. Res.*, 17(2002), No. 3, p. 701.